

Fabrication and Characterization of Graded Transition Joints for Welding Dissimilar Alloys

A GTAW system employing dual wire feeders was used to fabricate graded joints between 2.25Cr-1Mo steel and three austenitic alloys, and all cases showed a relatively smooth transition in composition

BY G. J. BRENTRUP and J. N. DuPONT

ABSTRACT

Functionally graded materials have potential for joining dissimilar materials in many applications. In this work, graded transition joints were fabricated for joining ferritic and austenitic alloys. A gas tungsten arc welding system employing dual wire feeders was used to fabricate graded joints between 2.25Cr-1Mo steel and three austenitic alloys, including IN800, IN82, and 347 stainless steel. All three joint combinations were characterized to determine compositional variations, microhardness profiles, and microstructural evolution. Tensile tests were also performed to evaluate the high-temperature mechanical properties. In all cases, a relatively smooth transition in composition was achieved over ~ 50 mm, which represents an increase in length of approximately three orders of magnitude compared to composition gradients observed in traditional dissimilar metal welds. Measured composition data from the transition joints were converted to Ni and Cr equivalents and used with the Schaeffler diagram to predict the phase distribution along the joints, and good agreement was obtained between the observed and predicted results. Peaks in hardness were observed along the joints and attributed to the formation of martensite. The tensile properties from 20° to 650°C were generally within the range of those expected for the end member alloys except for the T22-IN82 joint, which exhibited slightly lower yield and tensile strengths. Solidification cracking was observed in the T22-800 joints in the region that exhibited a fully austenitic solidification mode.

austenitic alloys. During fusion welding, the combination of the high alloy content of the austenitic filler metal and fast cooling rate produces a hard martensite band in the partially mixed zone (PMZ) (Refs. 2, 4, 5). High temperatures encountered during either postweld heat treatment (PWHT) or service provide the activation energy for carbon diffusion to occur down the chemical potential gradient from the ferritic steel toward the austenitic alloy (Refs. 1, 6–11). This can lead to formation of a soft carbon denuded zone near the interface on the ferritic steel, and nucleation and growth of carbides on the austenitic side that have very high hardness. These large differences in microstructure and hardness occur over very short distances across the weld interface (~ 50 – 100 μm) (Refs. 2, 6, 12). A band of carbides also forms along the weld interface in the ferritic side of the joint (Ref. 8). The difference in hardness across the weld interface increases with increasing aging time due to nucleation and growth of the interfacial carbides (Ref. 6). At the same time, strain is localized along the carbon denuded zone due to differences in creep strength (Refs. 13–15) while localized stresses develop due to differences in thermal expansion coefficients of the steels (Refs. 16, 17). As a consequence of the hardness and strength gradients, these stresses are concentrated in the weak carbon-depleted zone, generating creep voids around carbides that lead to eventual creep rupture (Refs. 16, 18).

There are two distinct morphologies of these carbides that can evolve in DMWs during aging (Refs. 1, 18–22). Type I carbides are the ones most frequently observed. These carbides form very close to the weld interface (~ 1 μm) in the HAZ of the ferritic steel. These carbides initially form with a spherical shape, but gradually acquire a lenticular morphology and can eventually form regions of continuous or semicontinuous carbides as they grow and coalesce. The Type II carbides generally form as a wide band and are associated

Introduction

Dissimilar metal welds (DMWs) between ferritic low-alloy steels and austenitic alloys are commonly used in power-generation plants. The less-expensive low-alloy steels are used in the low-temperature regions of the plant, while the higher temperatures in the superheater regions require the superior corrosion resistance and greater creep strength of more-expensive austenitic alloys. In a typical power plant, there can be thousands of DMWs, which are frequently cycled between room temperature and 650°C (Ref. 1). The DMWs are prone to premature failure due to differences in chemistry, thermal expansion, and creep strength between the two alloys (Refs. 1, 2). Premature failure of these DMWs can

result in forced plant outages that can cost a power company \$250,000–\$850,000 per day in lost revenue (Ref. 3). The failures occur from simultaneous metallurgical and mechanical factors, including development of strength gradients during both welding and service, formation of a weak carbon-depleted zone due to carbon migration, and concentration of stress from thermal cycling that causes accelerated creep failure.

The microstructure of DMWs in the as-welded condition consists of a sharp concentration gradient across the weld interface that separates the ferritic and

KEYWORDS

Cr-Mo Steels
Stainless Steels
Fracture
Graded Transition Joints

G. J. BRENTRUP and J. N. DuPONT (jnd1@lehigh.edu) are with the Dept. of Materials Science & Engineering, Lehigh University, Bethlehem, Pa.

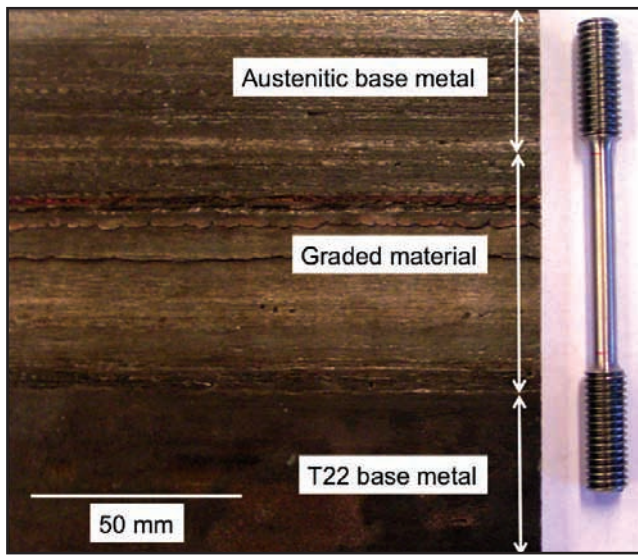


Fig. 1 — Picture of a T22 plate that had 50 layers of T22-Alloy 800 graded material added through the GTAW process to create graded joints, which were subsequently machined into the tensile bar geometry shown on the right.

with the martensite region that forms within the PMZ. For DMWs prepared with nickel-based filler metals, the Type I carbides that form along the interface provide sites for nucleation and growth of creep cavities that eventually lead to premature cracking. For older DMWs made with stainless steel filler metals, cracking typically occurs along the prior austenite grain boundaries (PAGBs) in the ferritic HAZ at a location of about one or two grains away from the weld interface.

Several different approaches have been taken to extend the service life of DMWs. Nickel-based filler metals reduce the coefficient of thermal expansion (CTE) mismatch between the austenitic and ferritic steels. Due to the low solubility and low diffusivity of carbon in Ni-based alloys, carbon migration is reduced over the service life of the weld (Refs. 6, 9, 19, 23, 24). The Ni-based fillers can improve the weld lifetime by a factor of five compared to austenitic filler metals (Ref. 23).

Another approach is to separate the carbon and stainless steels with a material of intermediate thermal expansion, known as a trimetallic joint. Several nickel-based alloys, notably Inco Alloy 800/800H, have a CTE intermediate between the two steels and have been used as suitable candidates. Studies on trimetallic joints (Refs. 19, 25, 26) have shown a fourfold increase in the lifetime and a 38% reduction in stress compared to traditional DMWs. However, failure has still been observed, indicating that the steep CTE, microstructure, and property gradients are still problems.

Building on the idea of the trimetallic joint, graded transition joints could be de-

veloped to replace DMWs with an intermediate section in which the composition varies continuously along its length. The graded joint smoothly transitions from the ferritic steel composition to the stainless steel composition, allowing two similar welds to replace the one dissimilar weld. By continuously grading the composition, the sharp changes in both composition and properties of traditional DMWs would be extended over the whole length of the component, potentially eliminating many of the factors that promote failure.

Functionally graded steels have been produced by a number of different research groups. Mohandesi et al. (Refs. 27, 28) have used transport processes, specifically diffusion of alloying elements, to produce functionally graded steels with layers of ferrite, austenite, bainite, and martensite. Coco et al. (Ref. 29) created graded Fe-C and Fe-Mn-C steels by partial decarburization. While these techniques appear to work well for low-alloy and carbon steels, compositional control of high-alloy steels and other alloys requires other methods. A preliminary study by Farren et al. (Ref. 30) demonstrated that a functionally graded material (FGM) that transitioned from carbon to stainless steel could be fabricated by the Laser Engineered Net Shaping (LENS) process. The FGM exhibited a gradual change in microstructure and hardness, indicating the sharp gradients in DMWs can be eliminated.

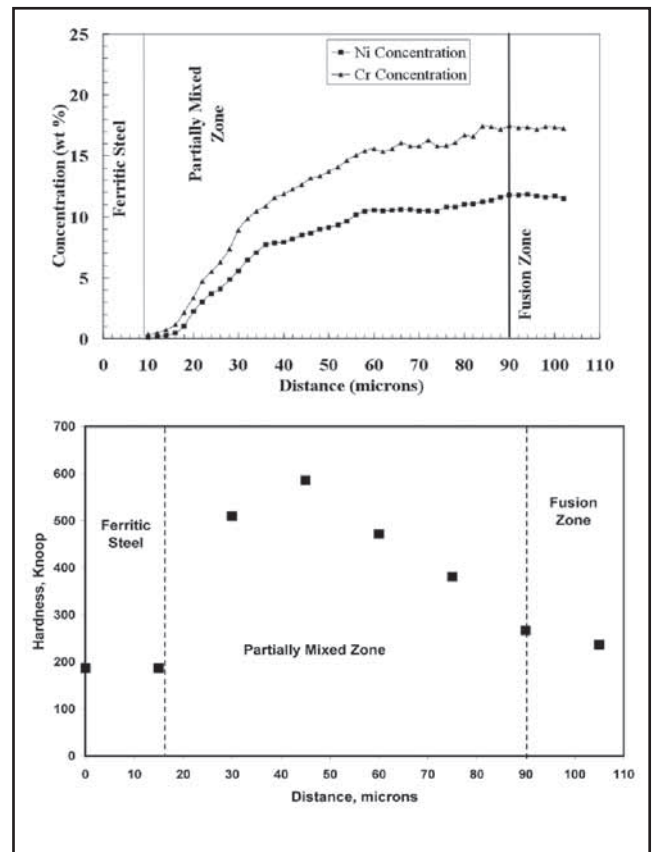


Fig. 2 — EDS composition (top) and hardness traces of traditional DMW demonstrating the sharp gradients in composition and properties (Ref. 4).

This paper describes the fabrication, characterization, and testing of graded joints with a smooth transition in composition, microstructure, and properties that can be used for joining ferritic alloys to austenitic alloys. The transition joints were fabricated by a dual-wire gas tungsten arc welding process and characterized by optical and electron microscopy, hardness testing, and high-temperature tensile testing. Future applications of the graded joints are joining ferritic and austenitic alloys in the power generation industry.

Procedure

Three types of graded transition joints were fabricated: T22 steel to IN82, T22 steel to IN800, and T22 steel to 347 stainless steel. These combinations were selected based on previous experience and their use in fossil-fired power plants. Most DMWs are currently welded with IN82 filler metal, and IN800 is often used as an intermediate section between ferritic and austenitic steels to reduce the CTE gradient. The T22 - 347 grade was explored to understand the behavior of a direct transition between a ferritic and austenitic steel.

Although the LENS system is useful for making graded transition joints (Ref.

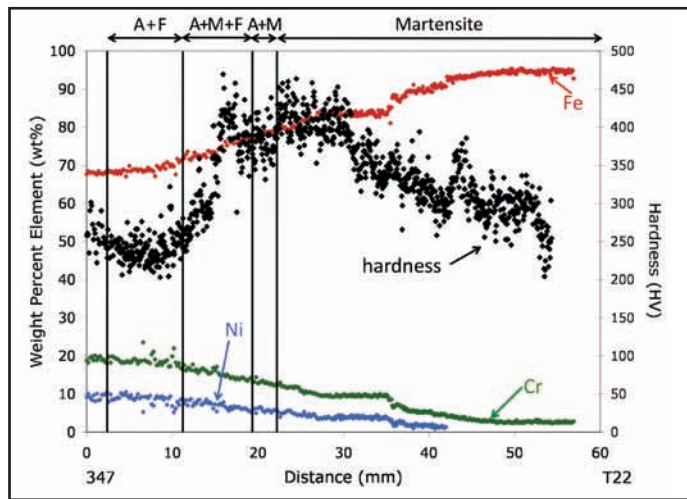


Fig. 3 — Plot of EDS and microhardness data as a function of distance for an as-welded T22-347 graded joint. Vertical lines correspond to phase boundaries from the Schaeffler diagram (A – austenite, F – ferrite, M – martensite).

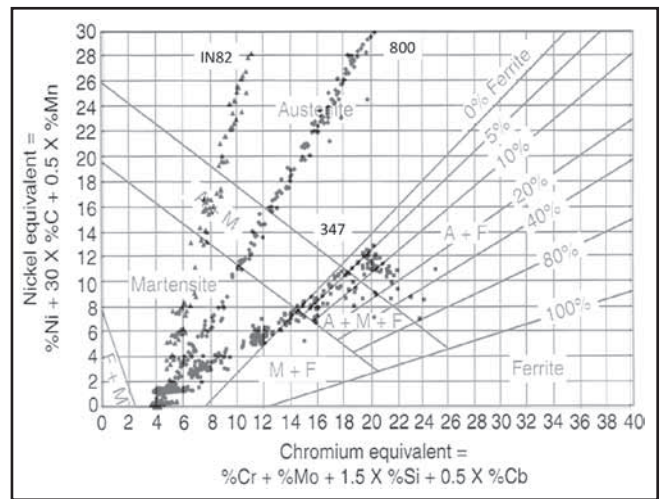


Fig. 4 — EDS composition data for each of the three graded joint combinations plotted as nickel and chromium equivalents on the Schaeffler diagram, which was used to determine the positions of the phase boundaries drawn as dark vertical lines in Fig. 3.

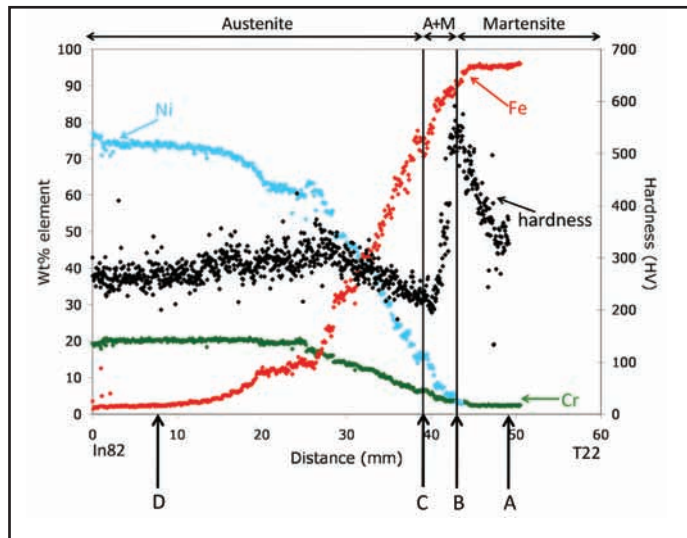


Fig. 5 — Plot of EDS and microhardness data for as-welded T22-IN82 graded joint. Vertical lines correspond to phase boundaries from the Schaeffler diagram (A – austenite, M – martensite). Lettered arrows correspond to locations of photomicrographs shown in Fig. 6.

30), several significant drawbacks of the LENS process have been recognized during the course of this work. First, the system is only capable of producing alloys from powders. Unfortunately, many alloys are not readily available in powder form, particularly for the size ranges required by the LENS powder feeders. Thus, fabrication of custom powders is typically required, which can be quite expensive. Second, previous research with the LENS process (Ref. 31) has shown that only about 5–14% of the powder is actually deposited, with the remaining being wasted. As a result, it is difficult to control the heat flow and deposit composition with powders because the precise amount of powder that enters into the liquid pool is un-

known. Last, the deposition rate of the LENS process is extremely slow, making fabrication of large parts impractical. Thus, a gas tungsten arc welding (GTAW) process using dual wire feeders was developed. In this system, wires rather than powders are used, so all of the material is fed directly into the melt pool and the composition can be more precisely controlled. In addition, the wires are more readily available and generally less expensive. The use of wire feeders

also allows for much higher deposition rates of ~3 kg/h compared to the LENS system with a deposition rate of only ~0.2 kg/h. All wire compositions are listed in Table 1. The diameter of the wires was 0.035 in. (0.9 mm). A 6.35 × 76.2 × 610 mm (0.5 × 3 × 24 in.) plate of T22 (2.25Cr-1Mo) steel (composition provided in Table 1) was clamped between two water-cooled copper plates. Material was deposited onto the edge of the T22 plate, and after each layer the copper plates were raised to ensure repeatable welds were made for each layer. The total feed rate of the two wires was maintained at a constant 1.27 m/min (50 in./min), and

individual wire speeds were varied with each new layer to adjust the composition and manufacture the grade. The first layer was deposited with the T22 and austenitic wire feed rates at 1.25 and 0.025 m/min (49 and 1 in./min), respectively. The second layer was deposited with the T22 filler metal at 1.22 m/min (48 in./min) and austenitic filler metal at 0.05 m/min (2 in./min). These changes continued until 50 layers were deposited. Once the grade was complete, two inches of additional “pure” austenitic material was deposited so that tensile bars could be machined with the entire grade contained in the gauge length of the test sample. A wire brush and ethanol were used to clean each layer after cooling. The welding parameters were a travel speed of 1 mm/s, a total wire feed rate of 1.27 m/min (50 in./min), a current of 250 A, a voltage of 13 ± 1 V, and a root opening of 6.35 mm (0.25 in.).

All graded joints were examined by radiographic X-ray analysis to detect any cracks or other defects. As shown in Fig. 1, tensile bars were machined from the plates so that the entire grade was contained in the reduced section. Tensile tests were performed at 20°, 250°, 350°, 450°, 550°, and 650°C in air using an extensometer at a strain rate of 0.127 mm/mm/min (0.005 in./in./min) through yield and then 1.27 to 2.54 mm/mm/min (0.05 to 0.10 in./in./min) to fracture. Two samples were tested at each temperature.

Additional samples were cut from the graded transition joints for metallographic analysis. The samples were mounted in cold-setting epoxy, ground using SiC papers, and polished using 6- and 1-μm diamond and 0.05-μm colloidal silica. The T22 half of the grade was etched using 2% Nital for 5–7 s. The alloy IN800 and IN82 halves were immersion

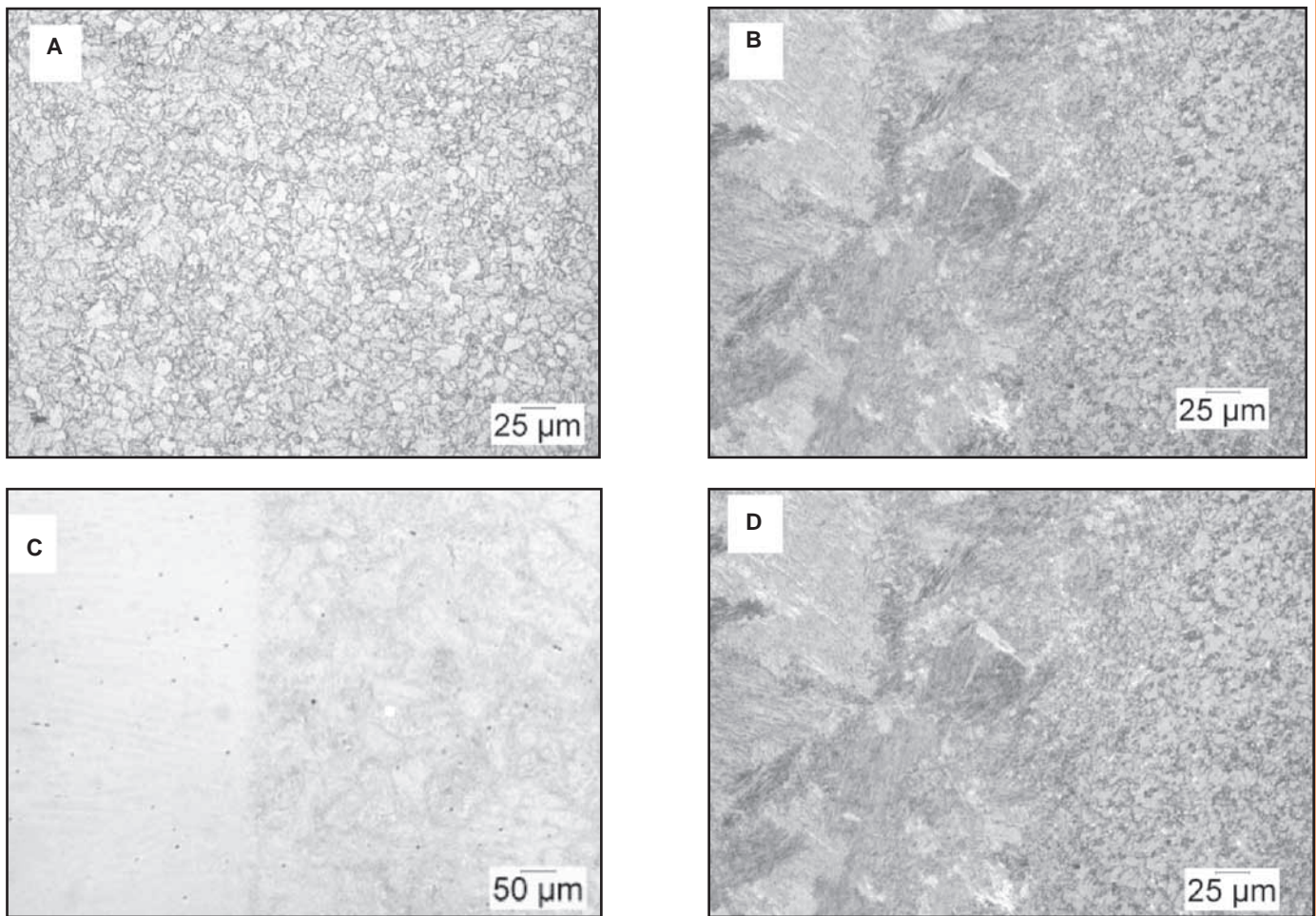


Fig. 6 — Representative photomicrographs from the T22-IN82 graded joint. Letters correspond to arrows in Fig. 5: A — Tempered martensite; B — transition between tempered martensite and lath martensite; C — transition between martensite and austenite; D — austenite.

etched with Marble’s reagent for 5–10 s, while the 347 half was electrolytically etched using Lucas’s reagent at 3 V for 15 s. Photomicrographs were recorded using an Olympus BH-2 optical microscope and Pax-It software. Microhardness measurements were performed on the graded joints using a Leco M400-FT hardness tester with a 10-g load, 15-s dwell time, and 50- μ m spacing between indents.

Energy-dispersive X-ray spectroscopy (EDS) composition analysis was conducted using a Hitachi 4300 FE scanning electron microscope (SEM) with an EDAX X-ray detector. An accelerating voltage of 20 kV was used for line scan measurements with 100- μ m spacing and

20-s dwell time. A set of standards of each material (T22, 347, 800, IN82) whose composition had been confirmed by wet chemical analysis was used for calibration of the EDS measurements.

Results and Discussion

As described previously, the sharp gradient in the composition, microstructure, and properties across the weld interface of DMWs between ferritic and austenitic alloys is the primary cause of premature failure. An example of the sharp concentration gradients in a conventional DMW is shown in Fig. 2 as a basis for comparison, where composition data are plotted as a

function of distance across the weld (Ref. 4). The primary alloying elements, nickel and chromium, both decrease sharply from 12 and 17 wt-% in the stainless steel to <1 wt-% in the ferritic steel. These composition changes occur over a distance of only ~80 μ m. The abrupt compositional changes lead to steep property gradients as well, as seen in the microhardness traverse in Fig. 2. The hardness increases from 200 Knoop in the ferritic steel to a maximum of 600 Knoop in the partially mixed zone before decreasing back to 250 Knoop in the stainless steel. The peak in hardness is associated with a band of martensite that forms along the weld interface.

Table 1 — Certified Compositions (wt-%) of the Alloy Wires Used to Construct the Graded Joints

Material	Al	C	Cr	Cu	Mn	Mo	Nb	Ni	Si	Ti	Fe
2.25Cr-1Mo	0.01	0.07	2.39	0.14	0.59	0.94	0.00	0.05	0.47	0.00	95.33
Alloy 800H	0.42	0.09	20.97	0.27	1.03	0.16	0.15	34.65	0.44	0.56	41.12
347	0.00	0.05	19.43	0.13	1.68	0.20	0.63	9.13	0.46	0.00	68.23
Inconel 82	0.00	0.10	20.00	0.50	3.00	0.00	2.50	67.00	0.50	0.75	3.00

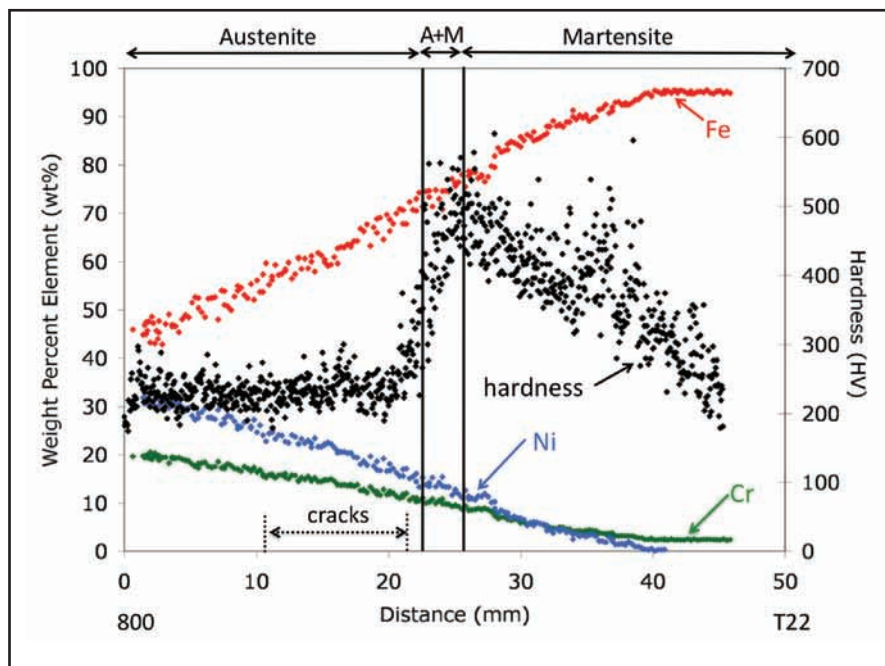


Fig. 7 — Plot of EDS and microhardness data as a function of distance for as-welded T22-800 graded joint. Vertical lines correspond to phase boundaries from the Schaeffler diagram (A – austenite, M – martensite).

The goal of graded transition joints is to eliminate these sharp composition and property gradients. Figure 3 shows microhardness and composition data for a T22-347 graded joint as a function of distance. Note the composition changes gradually over a distance of ~50 mm, compared to ~50–100 μm that is typically observed for conventional DMWs. The microhardness data also show that the sharp changes in hardness have been elongated over a much greater distance compared to traditional DMWs.

The expected distribution of phases along the joint can be understood by converting the composition data to chromium and nickel equivalents for use on the Schaeffler diagram (Ref. 32). For this, the concentration of major alloying elements was measured directly via EDS. Concentrations of carbon and minor alloying elements were determined with the approach previously described by DuPont and Kusko (Ref. 4). The dilution within each location was first calculated with the measured composition data of the major alloying elements. The concentration of carbon and minor alloying elements was then estimated by backcalculation from knowledge of the known dilution and filler metal compositions. Figure 4 shows the results plotted on the Schaeffler diagram (composition data for the other grades are also provided on this plot). Combination of the results shown in Figs. 3 and 4 permit estimation of the phase distribution within the joints, and these locations are

shown on the compositional plot in Fig. 3. Note that the increase in hardness that begins at ~9 mm corresponds reasonably well to the point in the grade where martensite is expected to form. The hardness then gradually decreases across the martensite region from ~400–450 HV at 20 mm to ~200 HV at 55 mm, which is the nominal hardness for T22.

Similar trends in the composition and microhardness data were observed for the T22-IN82 and T22-800 graded joints as shown in Figs. 5 and 7, respectively. These graded joints also have a gradual change in composition over ~50 mm. Light optical photomicrographs are provided in Fig. 6 for the T22-IN82 joint as an example of the microstructures observed in the graded joints. Each photomicrograph corresponds to one of the phase fields predicted by the Schaeffler diagram. The microstructure shown for the 50-mm location (Fig. 6A) consists of tempered martensite, as expected for the T22 end of the joint. The photomicrograph at 43 mm (Fig. 6B) shows the transition between the tempered martensite of the T22 base metal and the as-quenched lath martensite that forms where the composition begins to change. Figure 6C, at 38 mm, shows the transition between the austenite + martensite to the single-phase austenite region. Finally, the micrograph from 8 mm (Fig. 6D) corresponds to the austenitic microstructure observed for IN82. Similar microstructures were observed for the T22-347 and T22-800 joints.

Hardness peaks correspond to regions of the joints where the martensite phase is stable. The width of the martensite-containing regions varies for all three joints, from ~35 mm for the T22-347 to only ~10 mm for the T22-IN82. As described in previous work (Ref. 4), this is due to the variations in the width of the compositional gradients for each transition joint. The steepest concentration gradient occurs for the T22-IN82 joint, where the nickel and chromium contents decrease from 67 and 20 wt-%, respectively, in the IN82 down to <1 and 2 wt-% in the T22. This steep concentration gradient results in a relatively narrow martensite band, as seen in Fig. 5. Conversely, the T22-347 joint has a smaller gradient in composition and a wider martensite band — Fig. 3. The variation in the width of the martensite band is due to the variation in martensite start (M_s) temperature with composition (Ref. 4). It is known that alloying elements such as Ni, Cr, Mn, and Mo reduce the M_s temperature (Ref. 34). Thus, for the IN82, the large composition gradient pushes the M_s temperature below room temperature at a relatively short distance from the T22/graded joint interface. This stabilizes the austenite at a concomitantly short distance from the interface, producing a relatively thin martensite layer. In contrast, the relatively small concentration gradient of the T22/347 grade causes the M_s temperature to drop below room temperature at a larger distance from the interface, thus producing a larger martensite layer.

The hardness gradients observed in the transition joints occur over distances of ~5–10 mm and are considerably less severe than those observed in conventional DMWs in which the same hardness gradients occur over ~2–40 μm (Refs. 4, 6). The effect of the local hardness changes needs to be determined with long-term creep testing. Any possible detrimental effect may be minimized by more gradual changes in composition across the graded joint in the regions where martensite is known to form. This will be evaluated in future work.

Figures 8–10 show the tensile properties as a function of temperature for each of the graded joints. Also shown on the plots are minimum values (shown as solid lines) for the T22, 347, 800, and IN82 materials (elongation data are not available for the IN82 as deposited filler metal). A schematic tensile bar shows the failure locations as dotted lines for each test temperature, and the phase boundaries based on the variation in composition from the Schaeffler diagram are also indicated as solid vertical lines.

The ductility and yield strength results for the T22-347 and T22-IN800 grades fall within the range for the end member al-

loys, while the tensile strength is close to that of the lower strength material at each temperature. In general, yielding followed by eventual fracture is expected to occur in the weakest region of the joint. However, there are other factors to consider when interpreting tensile data from graded materials. For example, the overall yield strength can be increased due to constraint of deformation in a soft region from a hard neighboring region that restricts plastic flow. This could account for the yield strength of the graded joint being above that of the weaker alloy for the T22/347 and T22/800 transition joints. In addition, work hardening of the soft region can produce a shift of the fracture from the region of initial deformation to another region.

The data in Fig. 9 for the T22-IN82 joint demonstrate that this alloy combination exhibits yield and tensile strengths slightly below the nominal alloy properties. All of the failures occurred close to the T22 side of the joint, which may be attributed to the reduced tensile strength of T22 relative to IN82. The 20°C results shown in Fig. 9 are similar to those observed by Slaughter (Ref. 35) in DMWs between T22 and 304 stainless steel made with IN82 filler metal. The conventional T22-IN82-304 DMW exhibited yield and tensile strengths of 298 and 503 MP and failed in the T22 base metal. This is similar to the values of 300 and 490 MPa for the T22-IN82 graded joint that also failed very close to the T22 side of the joint.

The T22-800 graded joint exhibited solidification cracking as shown in the radiographs in Fig. 11 and light optical photomicrographs in Fig. 12. (Samples for tensile testing were extracted from crack-free locations.) The cracks are concentrated in an area of the X-ray that appears the lightest, indicating higher density associated with the fcc austenite phase. This light (high-density) region extends from 11 to 22 mm along the grade and, as shown in Fig. 7, occurs in the fully austenitic region. Also note that the cracks are located along the grain boundaries, which is typical for solidification cracks. It is well known that alloys that solidify as primary austenite are more prone to solidification cracking. Alloy 800 is not commonly used in filler metal form as done in this research. The results presented here indicate that further work would be required to identify the cause of cracking. Composition modifications may be needed before this alloy is used in a transition joint. At this point, it appears more appropriate to utilize the T22-IN82 transition joint in favor of the T22-800 combination in order to avoid this problem, since the IN82 end of the transition is compatible with many other austenitic alloys.

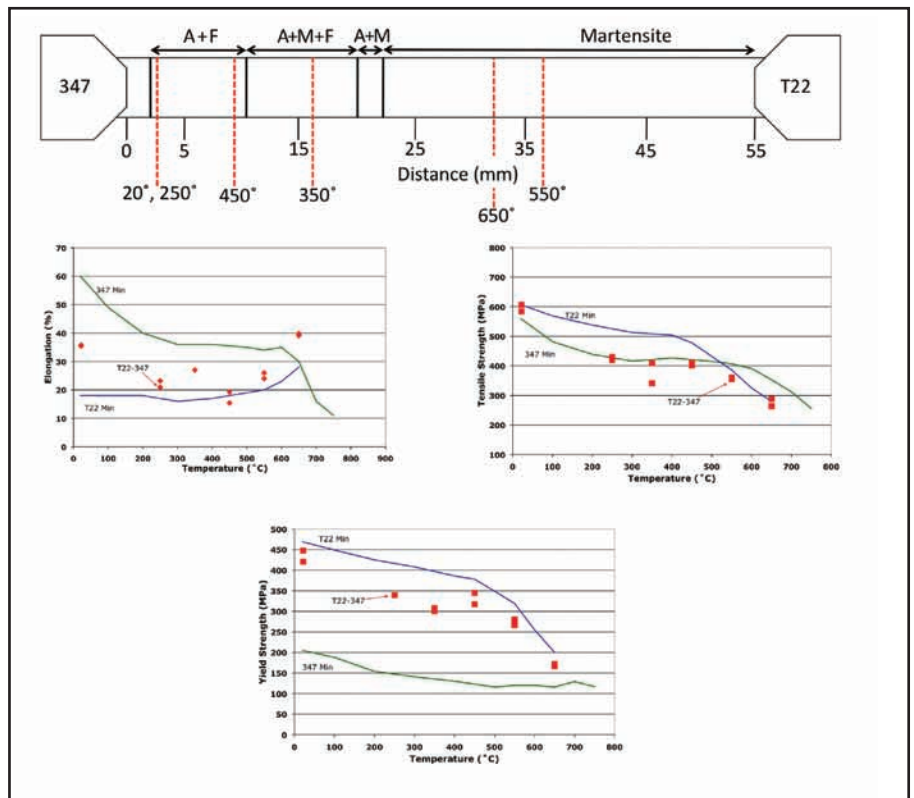


Fig. 8 — Plots of percent elongation, yield strength, and tensile strength as a function of temperature for a graded transition joint between T22 and 347. The minimum nominal alloy data (Refs. 13, 14, 36) are shown for comparison. The failure locations for each temperature are shown by the dotted lines on the schematic tensile bar above, along with the phase boundaries from the Schaeffler diagram.

Conclusions

Functionally graded transition joints were fabricated using a dual-wire GTAW process and used for microstructural and mechanical property characterization. The following conclusions can be drawn from this work.

1. The transition joints exhibited a smooth transition in composition over a distance of ~50 mm, which is significantly longer than the concentration differences typically observed in traditional dissimilar metal welds that occur over distances of ~50–100 μm .
2. Measured composition data from the transition joints were converted to Ni and Cr equivalents and used with the Schaeffler diagram to predict the phase distribution along the joints, and good agreement was obtained between the observed and predicted results.
3. Peaks in hardness were observed along the joints and were attributed to the formation of martensite.
4. The tensile properties from 20° to 650°C were generally within the range of those expected for the end member alloys except for the T22-IN82 joint, which exhibited slightly lower yield and tensile strengths.
5. Solidification cracking was ob-

served in the T22-800 joints in the region that exhibited a fully austenitic solidification mode.

Work is in progress to evaluate the aging and creep-rupture behavior of these joints and will be reported in future papers.

Acknowledgments

The authors gratefully acknowledge financial support through National Science Foundation Grant No. CMMI-0758622, the NSF Center for Integrated Materials Joining Science for Energy Applications, Grant IIP-1034703, PPL Corp., Contract 00474836, The Idaho Engineering Laboratory through Contract IIP-1034703, and the Pennsylvania Infrastructure Technology Alliance. Useful technical discussions with Ruben Choug and Robert Schneider of PPL Corp. and Ron Mizia and Mike Patterson of INL are also gratefully appreciated.

References

1. Campbell, G., Elmer, J., and Gibbs, W. 1981. Evaluation of factors controlling high temperature service life of 2-1/4 Cr-1 Mo steel to austenitic stainless steel weldments. *Trends in Welding Research in the United States* pp. 443–470.
2. Klueh, R. L., and King, J. F. 1982.

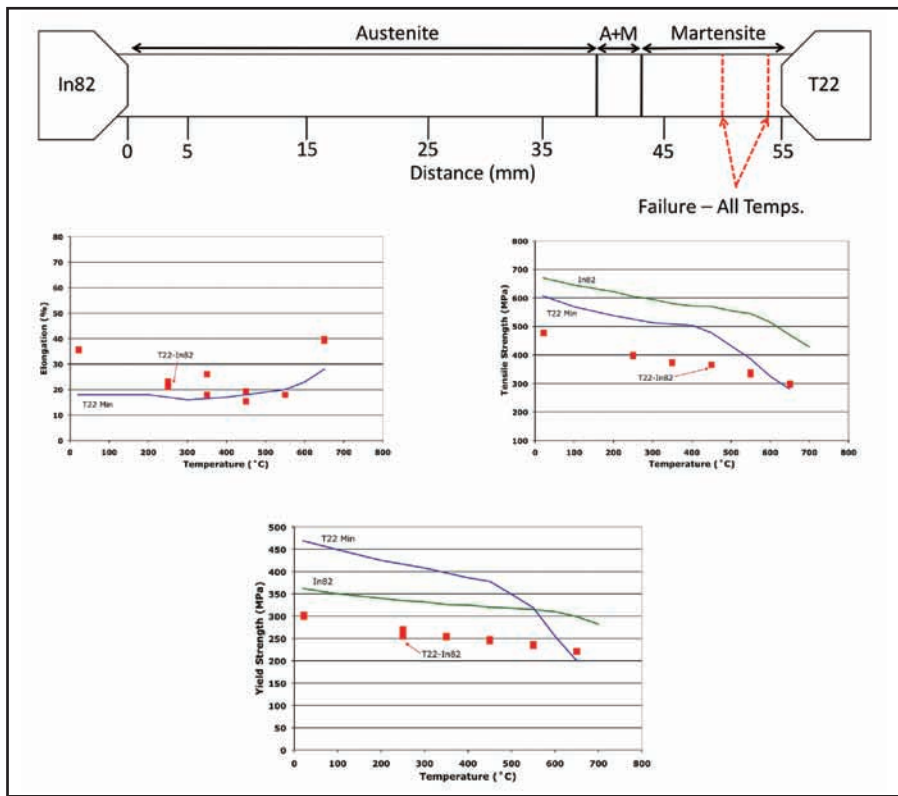


Fig. 9— Plots of percent elongation, yield strength, and tensile strength as a function of temperature for graded transition joints between T22 and IN82. The minimum nominal alloy data (Refs. 13, 37) are shown for comparison (except percent elongation data for IN82). All failures occurred within the dotted lines on the schematic tensile bar above. Also shown are the phase boundaries from the Schaeffler diagram.

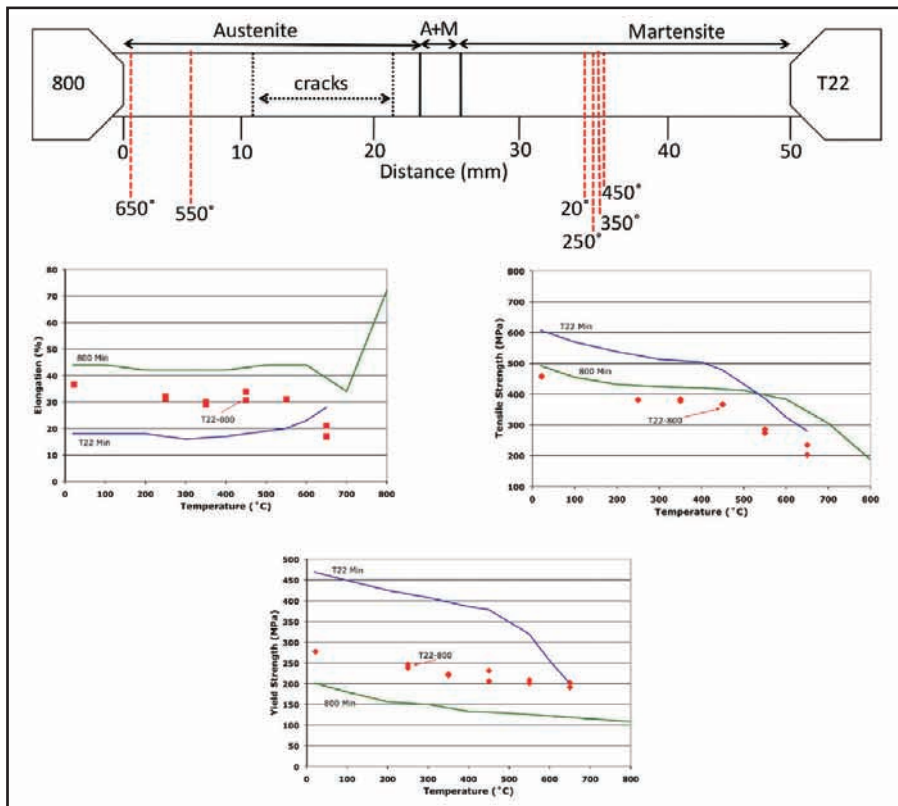


Fig. 10— Plots of percent elongation, yield strength, and tensile strength as a function of temperature for a graded transition joint between T22 and Alloy 800. The minimum nominal alloy data (Refs. 13, 38–40) are shown for comparison. The failure locations for each temperature are shown by the dotted lines on the schematic tensile bar above, along with the phase boundaries from the Schaeffler diagram.

Austenitic stainless steel-ferritic steel welded joint failures. *Welding Journal* 61(9): 302-s to 311-s.

3. Dooley, R., and Chang, P. 1997. The current status of boiler tube failures in fossil plants. *International Conference on Boiler Tube Failures in Fossil Plants*, Nashville, Tenn.

4. DuPont, J., and Kusko, C. 2007. Technical note: Martensite formation in austenitic/ferritic dissimilar alloy welds. *Welding Journal* 86(2): 54-s to 57-s.

5. Bala Srinivasan, P., and Satish Kumar, M. 2008. Characterization of thin section dissimilar weld joint comprising austenitic and ferritic stainless steels. *Materials Science and Technology* 24: 392–398.

6. Gittos, M., and Gooch, T. 1992. The interface below stainless steel and nickel-alloy claddings. *Welding Journal* 71(12): 461-s to 472-s.

7. Sireesha, M., Albert, S. K., and Sundaresan, S. 2005. Influence of high-temperature exposure on the microstructure and mechanical properties of dissimilar metal welds between modified 9Cr-1Mo steel and Alloy 800. *Metallurgical and Materials Transactions A* 36A: 1495–1506.

8. Laha, K., et al. 2001. An assessment of creep deformation and fracture behavior of 2.25Cr-1Mo similar and dissimilar weld joints. *Metallurgical and Materials Transactions A* 32: 115–124.

9. Eckel, J. F. 1964. Diffusion across dissimilar metal joints. *Welding Journal* 43(4): 170-s to 178-s.

10. Christoffel, R., and Curran, R. 1956. Carbon migration in welded joints at elevated temperatures. *Welding Journal* 35: 457-s to 468-s.

11. Gauzzi, F., and Missori, S. 1988. Microstructural transformations in austenitic-ferritic transition joints. *Journal of Materials Science* 23: 782–789.

12. Lundin, C. D. 1982. Dissimilar metal welds-transition joints literature review. *Welding Journal* 61(2): 58-s to 63-s.

13. *Data Sheets on the Elevated-Temperature Properties of Quenched and Tempered 2.25Cr-1Mo Steel Plates for Pressure Vessels (ASTM A542/A542M)*. 2003. 1-3 (National Research Institute for Metals, Japan).

14. *Data Sheets on the Elevated-Temperature Properties of 18Cr-12Ni-Nb Stainless Steel Tubes for Boilers and Heat Exchangers (SUS 347H TB)*. 2001. 1-3 (National Research Institute for Metals, Japan).

15. Nath, B. 1982. Creep rupture and creep crack growth behavior of transition joints. *International Conference on Welding Technology for Energy Applications* pp. 597–621.

16. Parker, J. D. 1994. High temperature failure of thick-section, low alloy steel to stainless steel transition weld. *Materials at High Temperatures* 12: 25–33.

17. Tucker, J., and Eberle, F. 1956. Development of a ferritic-austenitic weld joint for steam plant application. *Welding Journal* 35: 529-s to 540-s.

18. Parker, J. D., and Stratford, G. C. 2001. The high-temperature performance of nickel-based transition joints: I. Deformation behavior. *Materials Science and Engineering A* 299: 164–173.

19. Parker, J., and Stratford, G. 1999. Review of factors affecting condition assessment of nickel based transition joints. *Science and Technology of Welding & Joining* 4: 29–39.

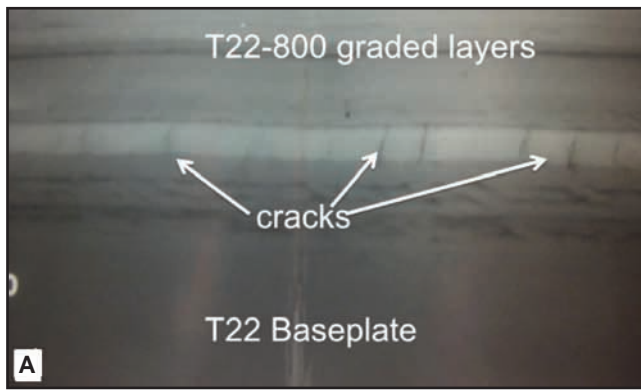


Fig. 11 — X-ray radiographs of as-welded T22-800 graded joint showing evidence of solidification cracking: A — Light-colored (more dense) region showing cracks throughout that region of the grade; B — close-up view of the cracks.

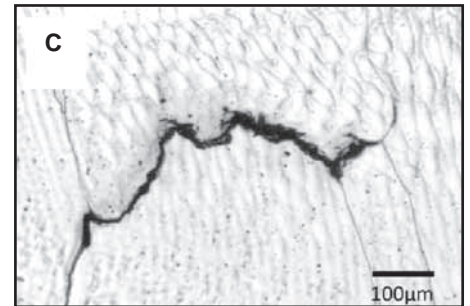
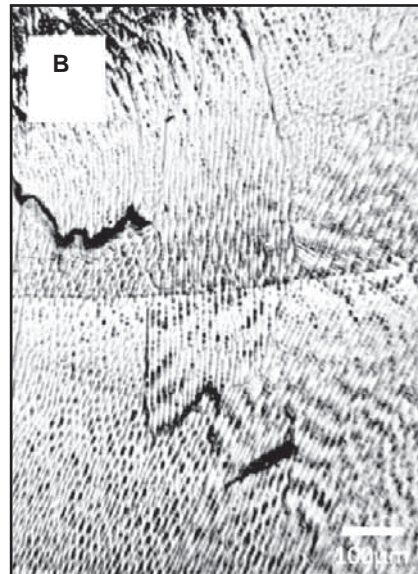
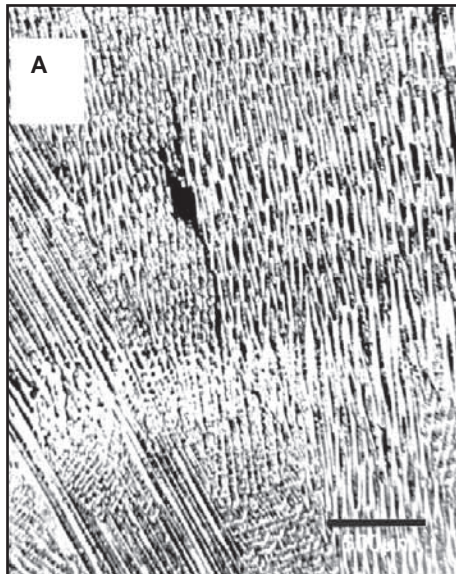


Fig. 12 — Light optical photomicrographs of solidification cracks in T22-800 graded joint.

20. Parker, J. D., and Stratford, G. C. 2001. The high-temperature performance of nickel-based transition joints: II. Fracture behavior. *Materials Science and Engineering A* 299: 174–184.

21. Ryder, R., et al. 1984. Dissimilar metal weld failures in power plants — Causes and remedies. *Trends in Electric Utility Research*.

22. Roberts, D., Ryder, R., and Viswanathan, R. 1985. Performance of dissimilar welds in service. *Journal of Pressure Vessel Technology* 107: 247–254.

23. Williams, J. A., and Parker, J. D. 1994. Effect of thermal cycling on creep behavior of 2.25Cr-1Mo/Type 316 steel dissimilar metal welds. *Materials Science and Technology* 10: 915–923.

24. Jones, W. 1974. Heat treatment effect on 2CrMo joints welded with a nickel-base electrode. *Welding Journal* 53(5): 225-s to 231-s.

25. King, J. F., Sullivan, M. D., and Slaughter, G. M. 1977. Development of an improved stainless steel to ferritic steel transition joint. *Welding Journal* 56(11): 354-s to 358-s.

26. Bhaduri, A. K., et al. 1992. Performance of a trimetallic transition joint. *Materials at High Temperatures* 10: 45–50.

27. Mohandesi, J. A., and Shahosseine, M. H. 2005. Transformation characteristics of functionally graded steels produced by electroslag

remelting. *Metallurgical and Materials Transactions A* 36A: 3471–3476.

28. Mohandesi, J. A., Shahosseine, M. H., and Namin, R. P. 2006. Tensile behavior of functionally graded steels produced by electroslag remelting. *Metallurgical and Materials Transactions A* 37A: 2125–2132.

29. Coco, L., et al. 2008. The mechanical response of compositionally graded materials. *Materials Science and Engineering: A* 483–484: 266–269.

30. Farren, J. D., DuPont, J. N., and Noecker, F. 2007. Fabrication of a carbon steel-to-stainless steel transition joint using direct laser deposition — A feasibility study. *Welding Journal* 86: 55-s to 61-s.

31. Unocic, R., and DuPont, J. 2004. Process efficiency measurements in the laser engineered net shaping process. *Metallurgical and Materials Transactions B* 35: 143–152.

32. Scheaffler, A. 1949. Constitution diagram for stainless steel weld metal. *Metal Progress* 56: 680.

33. Regina, J., DuPont, J., and Marder, A. 2007. The effect of chromium on the weldability and microstructure of Fe-Cr-Al weld cladding. *Welding Journal* 86(6): 170-s to 178-s.

34. Grange, R., and Stewart, H. 1946. *Trans. AIME* 167: 467–490.

35. Slaughter, G. M., and Housley, T. 1964. The welding of ferritic steels to austenitic stainless steels. *Welding Journal* 43(10): 454-s to 460-s.

36. *Data Sheets on the Elevated-Temperature Properties of 18Cr-10Ni-Nb Stainless Steel Tube for Boilers and Heat Exchangers (ASME SA-213/SA-213M Grade TP347HFG)*. 2010. 1-2 (National Research Institute for Metals, Japan).

37. Klueh, R. L., and King, J. F. 1977. *Elevated-Temperature Tensile Properties of ERNiCr-3 Weld Metal*. Oak Ridge, Tenn.: Oak Ridge National Laboratory.

38. *Data Sheets on the Elevated-Temperature Properties of Iron Based 21Cr-32Ni-Ti-Al Alloy for Heat Exchanger Seamless Tubes (NCF 800H TB)*. 1998. 1-2 (National Research Institute for Metals, Japan).

39. *Data Sheets on the Elevated-Temperature Stress Relaxation Properties of Iron Based 21Cr-32Ni-Ti-Al Alloy for Corrosion-Resisting and Heat-Resisting Superalloy Bar (NCF 800H-B)*. 1999. 1-2 (National Research Institute for Metals, Japan).

40. *Data Sheets on the Elevated-Temperature Properties of Iron Based 21Cr-32Ni-Ti-Al Superalloy for Corrosion-resisting and Heat-resisting Superalloy Plates (NCF 800H-P)*. 2000. 1-2 (National Research Institute for Metals, Japan).